Hydrogen-induced softening and embrittlement in 316L stainless steel fabricated using laser-powder bed fusion

Shi-Hao Li [a, b, c, *], Dong-Hyun Lee [d], Yakai Zhao [e, *], Upadrasta Ramamurty [c, e]

[a] School of Materials Science and Engineering, Zhengzhou University, Zhengzhou 450001, China
[b] Henan Province Key Laboratory of Advanced Light Alloys, Zhengzhou University, Zhengzhou 450002, China
[c] School of Mechanical and Aerospace Engineering, Nanyang Technological University, Singapore 639798, Republic of Singapore
[d] Department of Materials Science and Engineering, Chungnam National University, 34134 Daejeon, Republic of Korea
[e] Institute of Materials Research and Engineering (IMRE), Agency for Science, Technology and Research (A*STAR), Singapore 138634, Republic of Singapore

*Corresponding authors: *e-mail address*: lishihao@zzu.edu.cn (S.-H. Li); zhao_yakai@imre.a-star.edu.sg (Y. Zhao)

Abstract: To investigate the effects of hydrogen (H) on the mechanical properties of 316L austenitic stainless steel (316L) additively manufactured using laser-powder bed fusion (L-PBF), tensile, nanoindentation, and micropillar compression tests were performed on samples in both the as-built (AB) and H-charged (HC) conditions. Microstructural characterization revealed that the electrochemical H charging exerted marginal effects on grains, phases, and overall dislocation densities of L-PBF 316L. However, the dislocation networks inherent to L-PBF 316L appear to disentangle upon H charging and are distributed more homogeneously through the matrix. Mechanical test results showed that H charging results in a marginal reduction in hardness and strength, indicating H-induced softening, possibly due to the elastic shielding effects of H that weaken the interactions between dislocations. The elastic shielding effect and the enhanced slip planarity, facilitate the H accumulation along slip bands and twins, promote H-enhanced localized plasticity, resulting cracking when a critical H concentration is reached. This, in turn, aids in H embrittlement mechanism that results in a significant loss in ductility upon H charging. A detailed discussion of all these micromechanisms is presented.

Keywords: Hydrogen, laser-powder bed fusion, yield strength, softening, embrittlement

1. Introduction

Hydrogen (H) has been reported to degrade the mechanical properties of various metallic materials, resulting in inferior ductility and lowered fracture toughness in materials exposed to the H environments, which is known as H embrittlement (HE) [1-3]. The austenitic stainless steels (SS) are less susceptible to HE due to the low H diffusivity and higher H solubility in them [4]. Hence, they are frequently employed for industrial applications wherein exposure to H is higher (such as in production, transportation, and storage of H either in gaseous or liquid form). Nevertheless, HE remains still as a key issue for austenitic SSs that are exposed to H for an extended period of time, especially for metastable austenitic SSs [5, 6]. In these steels, strain-induced martensite, which forms during the deformation, can enhance the H diffusion that leads to eventual HE [5, 6]. Besides the phase transformation, HE in austenitic SSs and other metallic materials have been rationalized using H-enhanced localized plasticity (HELP) [7-9], H-enhanced decohesion (HEDE) [10, 11] and H-enhanced strain-induced vacancy formation [12] mechanisms. Each of these mechanisms consider the interactions between H and the microstructural features (including vacancies, dislocations, impurities, twins, slip bands, grain boundaries, cracks, *etc*.) from the nanoscale to macroscale.

The microstructures of metallic materials manufactured using additive manufacturing (AM) are considerably more complex compared to their conventionally manufactured (CM) counterparts [13-15]. They are typically hierarchical in nature, with the microstructural length scales that could range from the nanometer to millimeter, including a high-density of dislocations (that often form networks along the cellular boundaries), segregation of some of the alloying elements to the cellular boundaries, cellular structures, columnar and equiaxed grains, melt pool boundaries that impart a mesostructured which reflects the printing strategy used, *etc*. [13-15]. These unique features have been reported to impart a superior mechanical performance to them, such as favorable combination of strength and fracture toughness [16, 17].

In the context of H effects on AM alloys, prior studies have shown they are promising candidates for long-term service in the H environments. For example, the

316L grade austenitic stainless steel (simply referred as 316L hereafter) processed by employing the laser-powder bed fusion (L-PBF) technique exhibits a higher resistance to H damage compared to the CM 316L [18]. This is attributed to the suppressed martensitic transformation upon H charging in it, which, in turn, enhances the corrosion resistance due to reduced martensite content in the microstructure. Similarly, Claeys *et al*. [19] reported that L-PBF 316L shows a higher resistance to H-assisted cracking and, therefore, lower HE sensitivity than the cold-rolled and annealed 316L. The difference in HE originates from the variations in microstructures of samples prepared using different methods. For instance, the L-PBF 304L austenitic stainless steel shows lower H diffusivity than its CM counterpart, which is attributed to the high-density of tangled dislocations in the former [20].

HE in CM alloys was extensively investigated and, hence, reasonably well understood [1, 2], which is not the case of for AM alloys. The unique microstructures of AM alloys, which could, in turn, have complex interactions with H, make it necessary to further investigate the effects of H on their mechanical properties. Keeping the above in view, we have investigated the effects of H on the plastic deformation behavior of L-PBF 316L. H was introduced into the as-built (AB) 316L through electrochemical charging. Tensile, nanoindentation, and micropillar compression tests were conducted on both AB and H-charged (HC) L-PBF 316L and the results are compared and mechanisms elucidated.

2. Materials and experiments

2.1 Block preparation and microstructure characterization

Gas atomized spherical pre-alloyed 316L 316L powders (commercially obtained from Höganäs AB) with the size range of 15–53 μm were employed for L-PBF using the SLM 500 system. The optimized processing parameters are as follows: laser energy of 240 W, scanning speed of 600 mm/s, hatch spacing of 100 μm, and layer thickness of 40 μm. Blocks with dimensions of 60 (length) × 30 (width) × 30 (height) mm^3 were prepared using the chessboard scanning strategy with the island size of 4 × 4 mm^2 and 67° rotation along successive layers. Small pieces of AB 316L blocks were machined

using electrical discharge machining (EDM). Their surfaces, whose normal is parallel to the building direction (BD), were polished following the standard metallographic methods with the final mirror polishing using the 0.04 μm colloidal silica suspension. Several pieces after polishing were etched using the V2A reagent (45.5% distilled water, 45.5% hydrochloric acid, and 9.0% nitric acid) for the microstructural characterization using scanning electron microscopy (SEM, JEOL 7800F) [21]. Electron backscatter diffraction (EBSD) was performed on both the AB and HC specimens to determine the grain structures and phases. In addition, EBSD was conducted on well-polished pieces to locate grains with <110> orientation, which were utilized to fabricate micropillars. Thus, all the pillars examined in this study are orientated along the <110> direction. Step sizes adopted for characterization of grains, phases, pillar orientation, and geometrically necessary dislocations (GND) were 0.5, 0.1, 0.1, and 0.05 μm, respectively. Transmission electron microscopy (TEM, JEOL 2100F) on both the AB and HC samples were carried out on thin foils with the diameter of 3 mm that were extracted using EDM and ground to a thickness of about 70 μm, followed by twin-jet electropolishing using the 10% nitric acid plus methanol electrolyte that was maintained at a temperature between −10 and −20 °C [21]. For TEM characterization on the deformed tensile samples, thin lamellae were extracted from the gauge surface of both the AB and HC samples using focused ion beam (FIB, Zeiss Crossbeam 540). All lamellae were thinned to about 100 nm and finally polished using ion beam with current of 50 pA and voltage of 2 kV to minimize the surface damage.

2.2 Electrochemical H charging and quantification

Electrochemical H charging was conducted in 1 mol/L NaCl solution containing 0.3 g/L NH_4SCN. Using a Pt plate as the counter electrode, the L-PBF 316L samples were charged under a constant current of 100 mA/cm^2 for 24 h at room temperature. Small pieces and foils after polishing were H charged, followed by EBSD and TEM characterizations to examine any charging-induced microstructural variations. Similarly, tensile coupons were mirror polished and then charged for subsequent mechanical tests. The micropillars, fabricated using FIB on small pieces, were charged

by immersing the entire pieces into the solution with the same charging parameters. All HC samples were immersed into distilled water for 3 min to remove any NaCl that may have adhered to the surface. The amount of absorbed hydrogen was measured by recourse to thermal desorption spectroscopy (TDS, Bruker G8 Galileo) at a heating rate of 400 °C/h. The TDS measurements and all the subsequent mechanical tests were conducted within ~1 h after H charging to minimize H outgassing.

2.3 Mechanical property characterization

Tensile samples were machined using EDM and then polished before tests. The gauge dimensions of the tensile coupons are 2 mm in length, 1 mm in width, and 0.3 mm in thickness. Due to rather limited H diffusion distance (as will be demonstrated later), a thickness of 0.3 mm was used so as to highlight the influence of H, if any. Tensile tests were conducted at a nominal strain rate of 3×10^{-4} s^{-1} on both the AB and HC L-PBF 316L samples. A laser extensometer was used for measuring the strain during the tensile tests. At least 3 tests were conducted for each condition.

Nanoindentation tests were performed using a Bruker TI 980 Triboindenter equipped with a Berkovich tip, under load-control mode with a loading/unloading rate of 1.6 mN/s and a peak load of 8 mN. For each sample, 50 nanoindentation tests with interspacing of 8 μm were performed.

Single crystal L-PBF 316L micropillars, with diameters, D, of 1, 2, and 3.5 μm, were fabricated employing the well-polished small pieces via FIB machining. The micropillars were prepared using an ion beam of 3 nA first, followed by reduced intensity of ion beam machining and an ion beam of 20 pA for the final pillar polishing to minimize taper angle and potential surface damage. All the pillars had an aspect ratio of 2 to 3 with taper angle smaller than 2°. EBSD mapping was performed on all of them before testing to confirm their <110> orientation. Both the AB and HC micropillars were compressed using Bruker TI 980 Triboindenter equipped with a flat-punch diamond indenter. Displacement-control mode with a nominal strain rate of 10^{-3} s^{-1} was utilized. At least 5 pillars were tested for each condition. The post-mortem characterizations of the deformation features of the pillar were performed by employing

both SEM and TEM.

3. Results

3.1 Microstructures of AB and HC L-PBF 316L

Figure 1 shows the grain structures and phase compositions of the AB and HC L-PBF 316L, obtained using EBSD. Figure 1(a) shows that the AB sample contains both equiaxed and elongated grains when viewed along BD. The scanning direction (SD) is indicated using the black arrow in Figure 1(a). Notably, the small islands overlap with certain misorientation along successive layers, accompanied by remelting of the already-deposited layer(s). This makes scanning tracks less distinguishable. The grains exhibit relatively random crystallographic orientations without any strong texture. Phase mapping performed with a lower step size of 0.1 μm, displayed in Figure 1(b), shows that the AB 316L consists of full face-centered cubic (FCC) phase, *viz*. austenite, without any body-centered cubic (BCC) phase. Some earlier work reported the appearance of ferrite (BCC) in the AB L-PBF 316L samples [22]. The absence of ferrite in our samples could be a result of the Ni segregation to the cell boundaries, which helps stabilize the austenite phase [21]. The HC sample exhibits a grain structure (Figure 1(c)) that is similar to that observed in the AB sample, with no perceptible difference in grain size, morphology, or orientation distribution. In addition, no phase transformation upon H charging could be identified in the HC 316L, as evidenced by Figure 1(d) suggesting a fully austenitic microstructure. H-charging-induced austenite to martensite phase transformation was reported in both conventionally manufactured (CM) and L-PBF austenitic stainless steels [18, 23, 24], which is attributed to various factors, including reduced stacking fault energy (SFE), stacking-fault-assisted martensite formation, stress-induced phase transformation, *etc*. However, it appears that none of these are operative here to trigger the phase transformation in the L-PBF 316L.

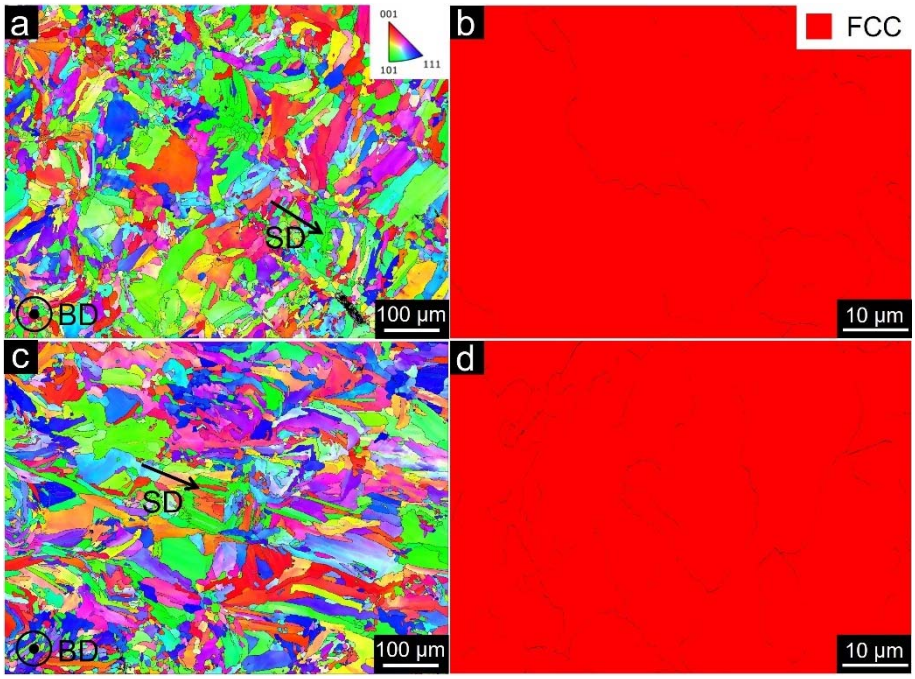

Figure 1. (a) EBSD map and (b) phase of AB 316L. (c) EBSD map and (d) phase of HC 316L.

The dislocation densities in the AB and HC 316L samples were estimated using EBSD conducted at lower step size of 0.05 µm. For an unbiased comparison, EBSD mapping was performed on the exact same region of one sample before and after H charging, as shown in Figures 2(a) and (c), respectively. Notably, to remove any potential electron beam irradiation damage resulting from the EBSD scanning, the AB sample was further polished slightly after EBSD, followed by H charging and subsequent EBSD mapping. The maps describing the GND densities shown in Figures 2(b) and (d) demonstrate that the AB and HC samples have comparable dislocation distributions and densities. The GND densities determined based on these maps are $2.15 \pm 1.12\times10^{14}$ and $2.24 \pm 1.15\times10^{14}$ m^{-2} in the AB and HC samples, respectively. It is important to note here that the estimated GND density corresponds to the minimum density of dislocations in the material, as it does not consider statistically stored dislocations. The similarities observed indicate that H charging does not alter the GND density in L-PBF 316L in any significant manner.

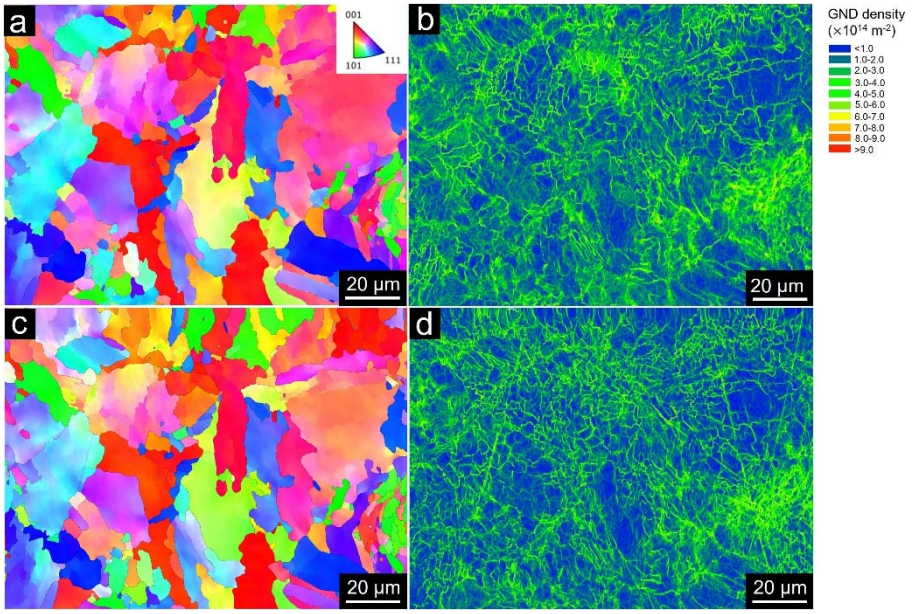

Figure 2. (a) EBSD and (b) GND density map of the AB 316L. (c) EBSD and (d) GND density map captured along the same area after H charging.

The cellular structures and dislocation networks in the AB and HC samples were further characterized using SEM and TEM, respectively. Figure 3(a) reveals that equiaxed cells prevail in the AB sample. The sharp contrast between the cell boundaries and the cell interiors comes from the elemental segregation, which leads to enhanced etching resistance of cell boundaries as compared to cell interiors [21]. The micrograph displayed in Figure 3(a) was captured in the secondary electron imaging mode. Well-organized dislocation networks, featured by heavily tangled and dense dislocation networks along the cell boundaries and relatively free of dislocations within their interiors, prevail in the AB 316L sample. Simulation studies have attributed the formation of such dislocation networks in the L-PBF alloys to the continuous thermal cycles (and the resultant mechanical loading cycles) exerted on the solidifying materials during the L-PBF process [25]. The HC L-PBF 316L sample shows cellular structures similar to that of the AB counterpart (Figure 3(c)) when imaged using the secondary electron imaging mode, in terms of both size and morphology. The imperceptible difference in features of cellular structures in the AB and HC indicates that H charging has negligible influence on the cellular structures as well. This is further supported by the EDS results on the HC 316L (as shown in Figure S1 of the Supplementary

Information, SI). They show that the cell boundaries in the HC sample are enriched in Cr, Ni, Mo, and Mn, which is the same as in the AB sample [21]. Although no significant difference in dislocation densities in the AB and HC 316L samples could be identified, it appears that dislocation networks evolve upon H charging and the morphology of dislocation networks in the HC sample differs from that in the AB counterpart. Typical TEM images showing the dislocation structures in the AB and HC thin foils are presented in Figures 3(b) and (e), respectively, for a direct comparison. The initially well-organized dislocations disentangle, to some extent, after being subjected to H charging, resulting in (somewhat) less closely packed dislocation distribution along the boundaries and some sparse dislocations within the interiors. The evolution of dislocation arrangements upon H charging is further highlighted by comparing TEM images obtained from the AB (Figure 3(c)) and HC (Figure 3(f)) thin foils captured at higher magnitude. The dislocations are organized into networks with in the AB sample, whereas they are distributed relatively homogeneously in the HC counterpart. The dislocation structure evolution indicates that dislocation activities (such as glide) were potentially triggered during H charging.

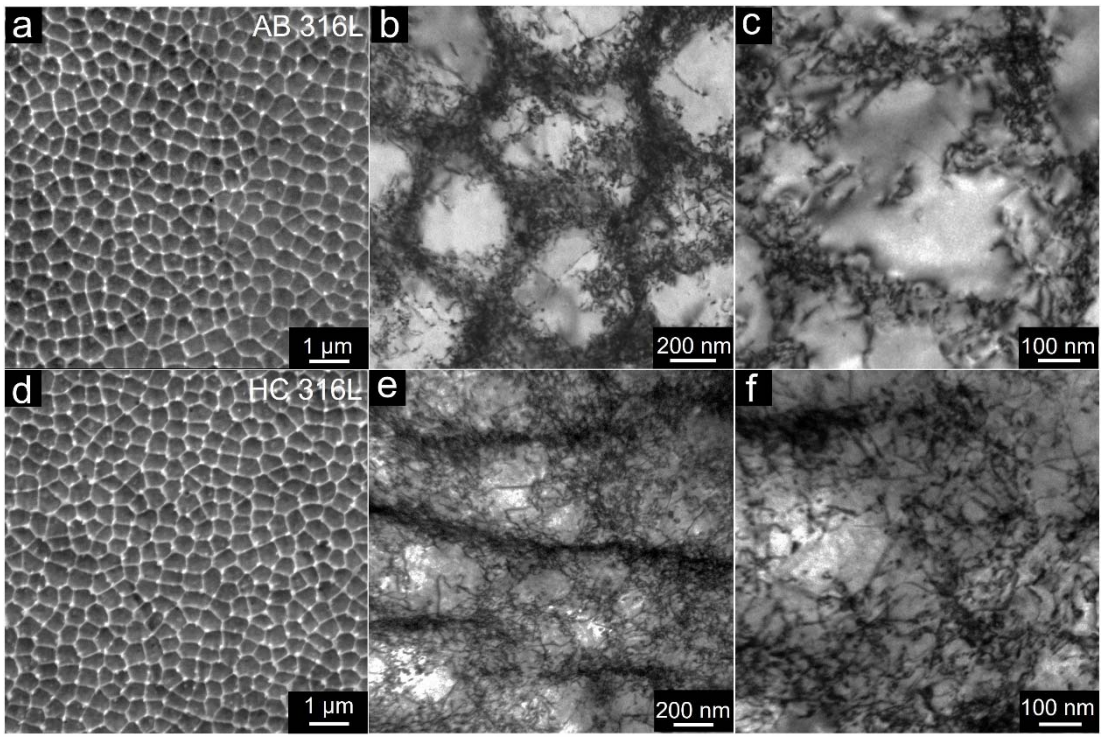

Figure 3. SEM images (using secondary electron imaging mode) of the cellular structures in the (a) AB and (d) HC L-PBF 316L samples. Corresponding TEM images of the dislocation networks in (b) and (c)AB (with the boundaries consisting of a high-density of tangled dislocations and interiors free of dislocations), and (e) and (f) HC (where dislocation networks are somewhat disentangled) samples.

To further check if the dislocation network evolution is a result of other factors related to the thin-foil TEM samples (such as image forces), instead of H charging, TEM samples extracted from the well-polished HC bulk pieces were prepared via FIB lift-out. Two typical TEM images captured at different locations of the FIB lift-out samples are shown in Figure 4(a) and (b), respectively. As shown in Figure 4(a), similar to those observed in the thin foils, the dislocation networks show blurry boundaries within the shallow region (within ~1.2 μm from the charging surface). Dislocations are distributed sparsely and homogeneously in this region. In contrast, well-organized dislocation networks could be identified with increasing depth. Similarly, no clear dislocation networks can be identified within a depth of about 1.2 μm in Figure 4(b), and dislocations are observed to distributed relatively homogeneously. The discrepancy in the dislocation structure morphologies of different regions implies that H charging could possibly activate dislocations in the L-PBF 316L sample, resulting in the dislocation disentanglement and relatively homogeneously distributed morphology. The results shown here match well with those in Figures 3(b) and (d), indicating that H charging is the key factor altering dislocation arrangements.

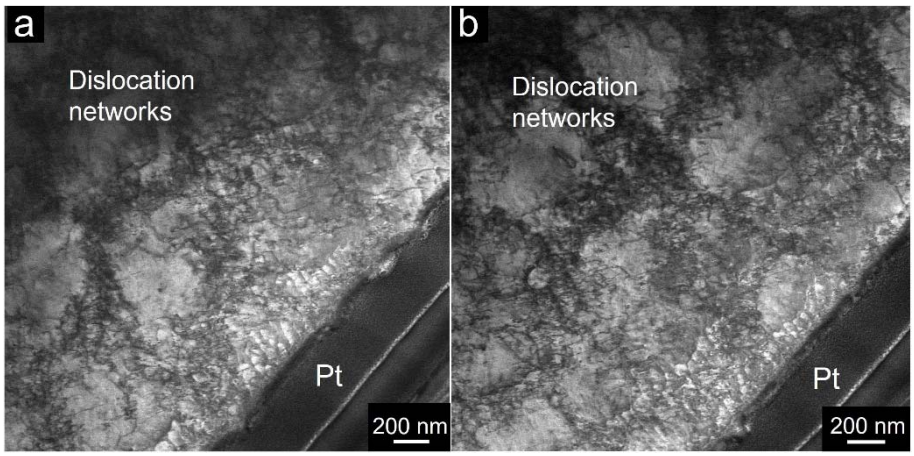

Figure 4. Typical TEM images on lamella of HC 316L. Dislocations along the very surface distribute relatively homogeneously, and dislocations organize into networks

with increasing depth from the surface.

3.2 Tensile tests on AB and HC L-PBF 316L

The typical tensile stress-strain responses of the AB and HC 316L samples are shown in Figure 5. Compared to the AB sample, the HC sample exhibits inferior mechanical properties, manifesting as slightly lower yield strength (σ_Y) and largely reduced elongation to failure (ε_f). Their average values are listed in Table 1, which shows that the reduction in σ_Y due to H charging is marginal (about 20 MPa, which is less than 4%), whereas ε_f deteriorates significantly (by about 30% of that in the AB sample), indicating high HE susceptibility. (Note that σ_Y and ε_f of the AB 316L samples (with ~0.3 mm thickness) are similar to those reported on much thicker specimens, in prior studies [26, 27], indicating that the ultrathin specimens exhibit similar responses to the bulk ones.) A slight reduction in σ_Y but a dramatically decreased ε_f demonstrate that, compared to the strength, the plasticity of L-PBF 316L is more severely affected by H charging. The HE susceptibility of materials can be quantified using the ratio of ε_f of the HC sample to that of the AB counterpart [28], which is ~0.7 here.

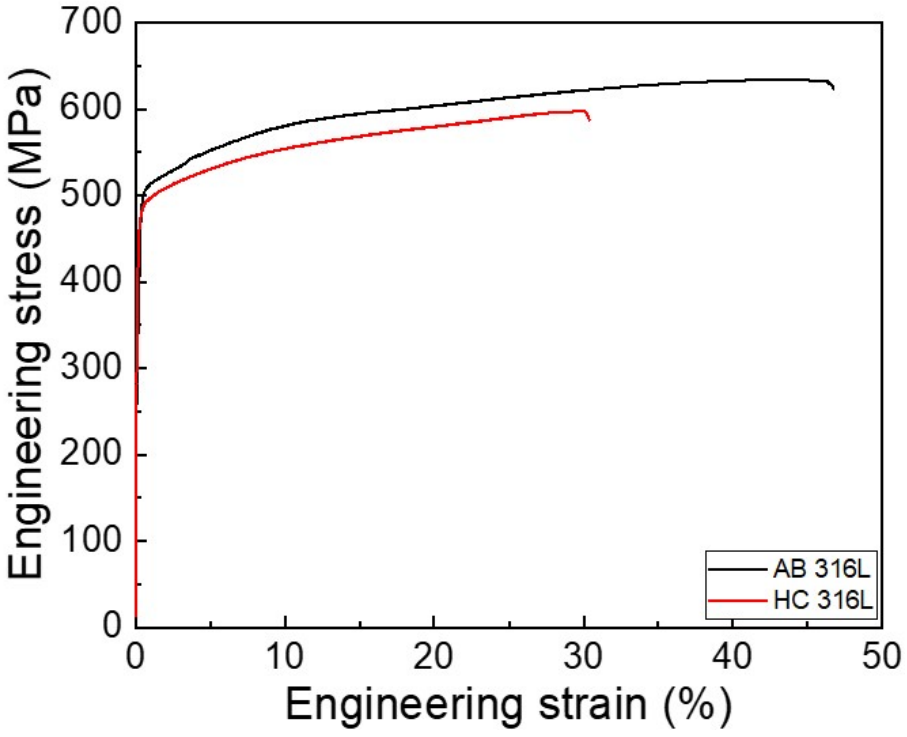

Figure 5. Typical stress-strain responses of AB (black curve) and HC (red curve) 316L.

Table 1 Tensile properties of AB and HC 316L

Sample	Yield strength, σ_Y(MPa)	Elongation, ε_f(%)
AB 316L	516±17	45.4±5.0
HC 316L	495±14	31.8±4.7

3.3 Nanoindentation and micropillar compression tests

The slightly reduced σ_Y in the HC 316L indicates softening induced by charging. For the electrochemical charging conditions employed in this study, the H-affected zone is typically limited to the surface region with the thickness of a few micrometers [29], and hence the nanoindentation technique probing micro or even nanometer length scale is appropriate in revealing such localized H effects. Nanoindentation tests with a peak load of 8 mN were hence preformed on both AB and HC 316L, and the representative load-displacement curves are shown in Figure 6(a), where the larger depth indicates lower hardness upon H charging. The cumulative probability distributions of the hardness values are presented in Figure 6(b). The average hardness values of the AB and HC 316L 3.30±0.15 and 3.17±0.17 GPa, respectively, *i.e.*, a ~3.9% reduction in hardness occurs due to H charging, which is similar to that noted for σ_Y.

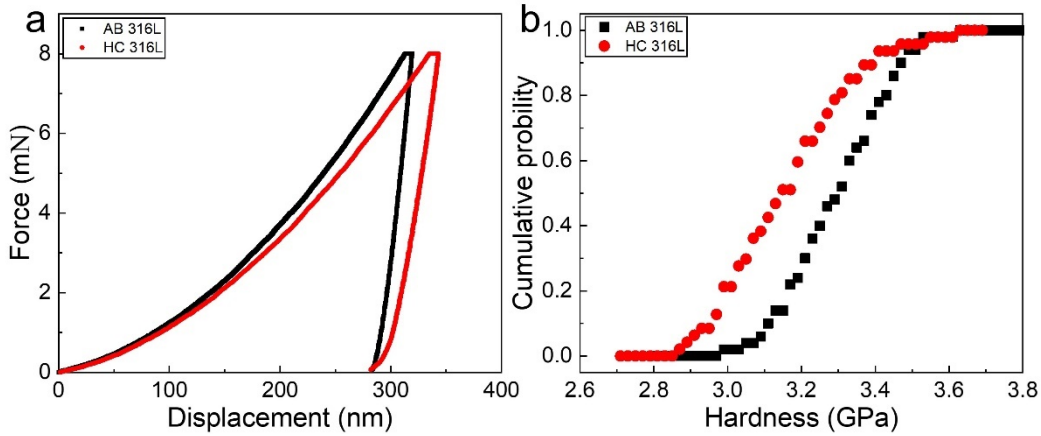

Figure 6. (a) Typical force-displacement curves of nanoindentation tests on AB (black curve) and HC (red curve) samples. (b) The cumulative probability distribution of the hardness values obtained on AB and HC 316L.

To further understand the H-induced softening behavior, micropillar compression

tests were conducted on single-crystalline pillars that are orientated along <110> (as shown in Figure S2). The typical stress-strain responses of pillars with D=2 μm are shown in Figure 7 (those of 1 and 3.5 μm are displayed in Figure S3). Compared to the AB pillars, all the HC pillars are featured by lower σ_Y (average values listed in Table 2), corresponding well with the lower σ_Y and nanohardness. In addition, H charging also deteriorates the work hardening capability of the micropillars [30]. As indicated by the dashed lines and summarized in Table 2, the work hardening rate θ of the AB pillar within the 2–5% plastic strain regime is ~3.61 GPa, which is significantly higher than that of the HC counterpart (~2.52 GPa). The 2-5% plastic strain was selected as micropillars show steady plastic deformation within the range [21, 31]. Note here that due to prevailing strain gradient [32], micropillars do not deform homogeneously during the compression tests, and, therefore, work hardening behaviors of micropillars are often evaluated using the engineering stress-strain curves [33].

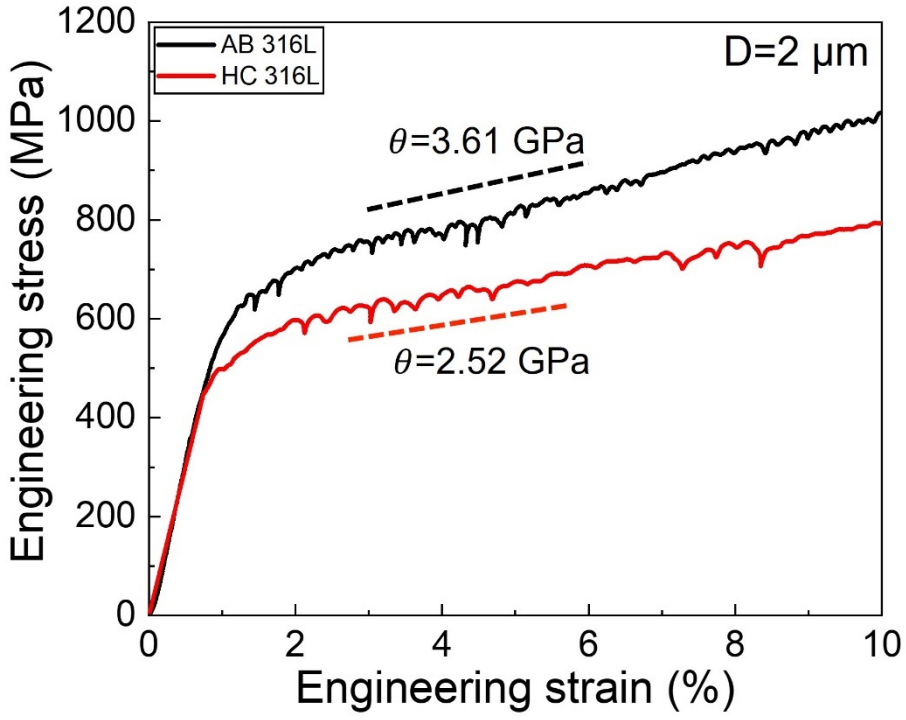

Figure 7. Typical stress-strain responses of AB (black curve) and HC (red curve) pillars with D=2 μm. The work hardening rates within the 2–5% plastic strain are calculated and indicated using dashed lines.

Table 2 The average yield strength σ_Y and work hardening rate θ of pillars in AB and HC conditions.

Samples	σ_Y (MPa)			θ (GPa)		
D (μm)	1	2	3.5	1	2	3.5
AB 316L	641±25	560±22	539±17	2.82±0.51	3.55±0.36	4.17±0.36
HC 316L	561±16	512±11	505±15	2.47±0.56	3.03±0.78	3.25±0.32

3.4 Microstructural evolution

The inferior strength/hardness and ductility that result from H charging are closely linked to the microstructural evolution that occurs during the plastic deformation. Additional interrupted tensile tests (till 5% strain) were therefore performed, followed by detailed microstructural characterizations. As seen in the SEM image in Figure 8(a), upon 5% tensile stain, both slip bands (indicated by black arrows) and twins (with the boundaries outlined using red lines) carry plasticity in the AB 316L. While some grains are dominated by slip bands, some others are featured by twins. As demonstrated by EBSD maps shown in Figure 8(b), the discrepancy in main deformation features is most likely resulted from variations in grain orientations. Quantitative analysis reveals that the fraction of the twin boundaries (*i.e.*, the ratio of length of twin boundaries to the length of grain boundaries plus twin boundaries) is ~10.8%. Figures 8(c) and (d) show that the HC 316L with 5% tensile strain exhibit deformation features similar to that of the AB counterpart, *i.e.*, both slip bands and twins are observed on the surface. The fraction of the twin boundaries is ~8.1%, similar to that in the HC sample.

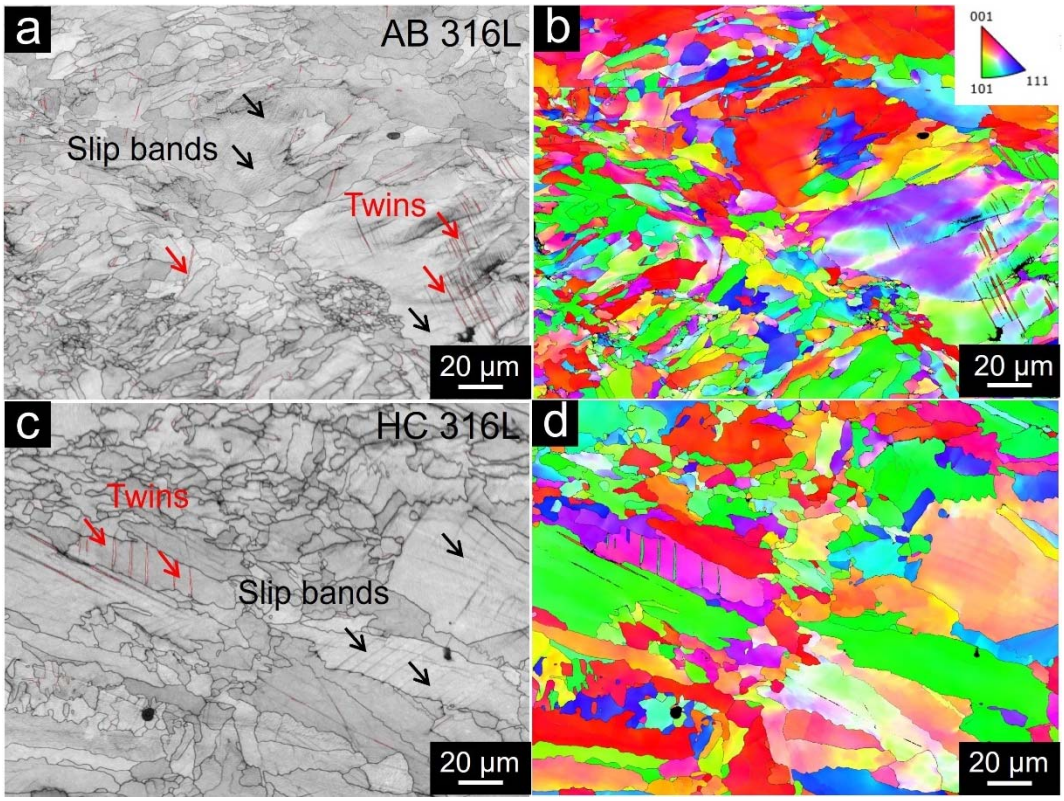

Figure 8. (a) SEM image and (b) EBSD map showing slip bands and twins in AB 316L with 5% tensile strain. Slip bands and twins in the deformed HC 316L characterized using (c) SEM image and (d) EBSD map.

Further microstructural characterizations were conducted using TEM on lamella samples prepared using the FIB lift-out technique. In the AB 316L, fine and closely packed slip bands (which were verified using the corresponding selected area diffraction pattern (SADP)) are observed when viewed along the [110] crystallographic direction (Figure 9(a)). The spacing of these slip bands is relatively small, ~0.10 μm based on the TEM images. Some slip bands cut through the cell boundaries and extend across several cells; this deformation feature was investigated in detail in a previous study by us [21]. In contrast, as shown in Figure 9(c), the slip bands in the HC 316L appear to be more sparsely distributed. (It is noteworthy that such difference in the slip bands between AB and HC samples is not from crystallographic orientation as the TEM images are all captured along the [110] zone axis.) The average spacing of the slip bands measured is ~0.53 μm, which is much larger than that in the AB sample. This indicates that the appearance of H-enhanced slip planarity [8, 9, 34], wherein cross slip is suppressed and dislocation motion gets restricted to a few slip planes [35]. In addition,

the dislocation networks in the HC samples are less well-organized, agreeing well with the observations of relatively homogeneous distribution of dislocations upon H charging seen in Figures 3 and 4.

In addition to the slip bands, deformation twins (that were verified using the corresponding SADP) were also frequently observed in both the AB and HC samples, as shown in Figures 9(b) and (d), respectively. Similar to the slip bands, the twins in the AB 316L are narrowly spaced, whereas they are widely spaced in the HC sample. It has been reported that H reduces the SFE of some metallic materials [36, 37]. However, in the present study, it seems that deformation twins are more prevalent in the AB 316L sample compared to the HC sample, as demonstrated by both higher volume fraction (Figure 8) and density (Figure 9) of twins in the former. This indicates that the reduced SFE due to H charging, if any, is rather limited in affecting the twining behavior here, whereas the slightly higher flow stress in the AB sample may be the more predominant factor facilitating the deformation twins.

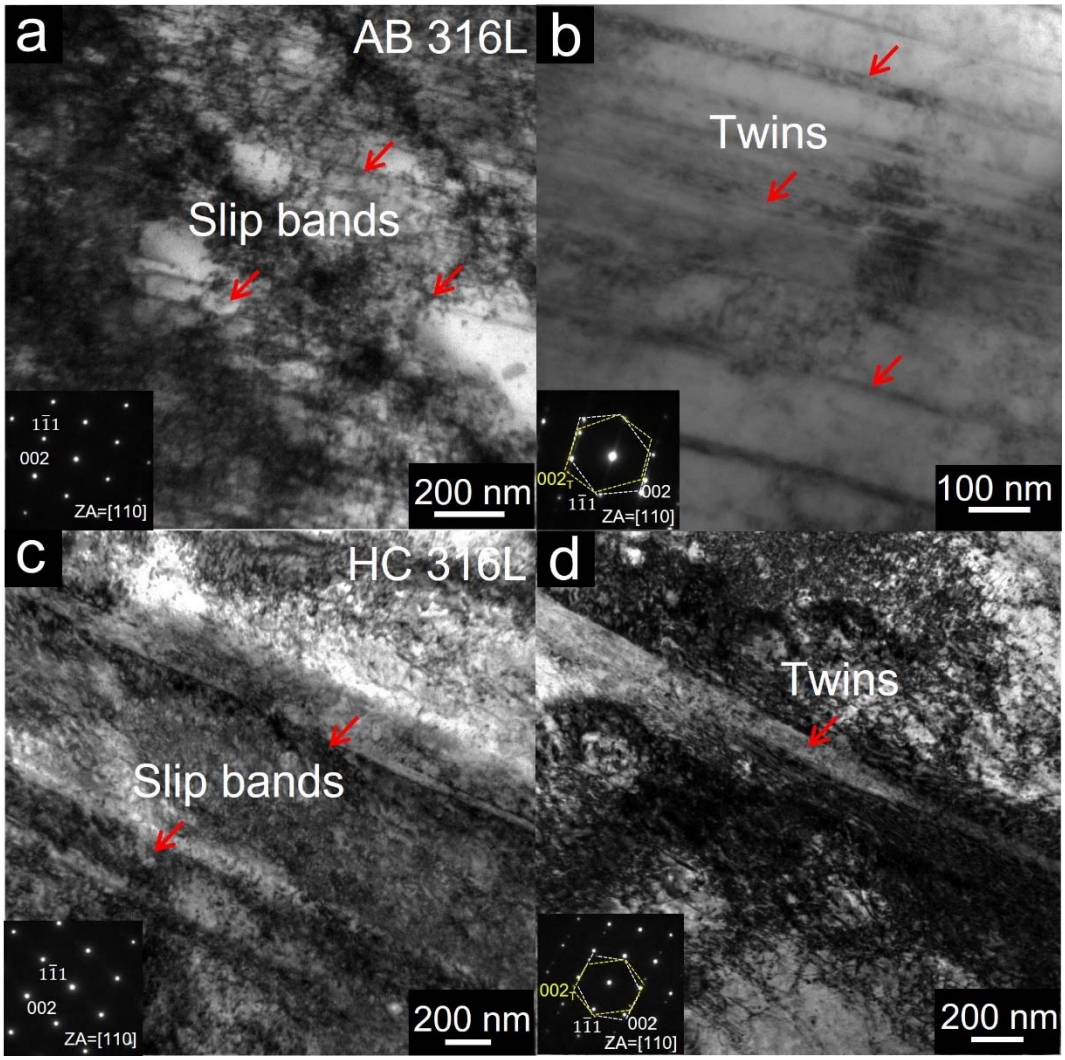

Figure 9. TEM images of (a) slip bands and (b) twins in the AB 316L with 5% strain. (c) slip bands and (d) twins in the 5% tensile deformed HC 316L.

In addition to the 5% pre-strained samples, tensile-fractured AB and HC samples were also characterized using SEM with the representative fractographs shown in Figure 10. Two different features in the fracture morphologies are notable. 1) In the AB 316L sample, typical slip bands and twins (as will be proven later) were present in regions near the fracture surface (Figure 10(a)). In the HC sample, in contrast, cracks, with their long axes approximately perpendicular to the loading direction (indicated by the white arrows), are frequently observed (Figure 10(c)). A few cracks propagating along the slip bands and twin boundaries were also identified as indicated by the yellow dashed lines. 2) The fractured surface of the AB 316L sample shows a more homogeneous morphology and is featured by void sheet consisting of dense submicron-

scale voids/dimples [38], i.e., the characteristics of ductile fracture. However, the fractured surface of the HC 316L sample consists of two distinct regions; quasi-cleavage fracture feature (indicating brittle fracture) is dominant from the surface to a depth of ~6–7 μm (viz. surface region) whereas void sheet is identified with further increasing depth (inner region). The thin brittle region near surface is developed because H is highly concentrated near surface under electrochemical charging condition [39].

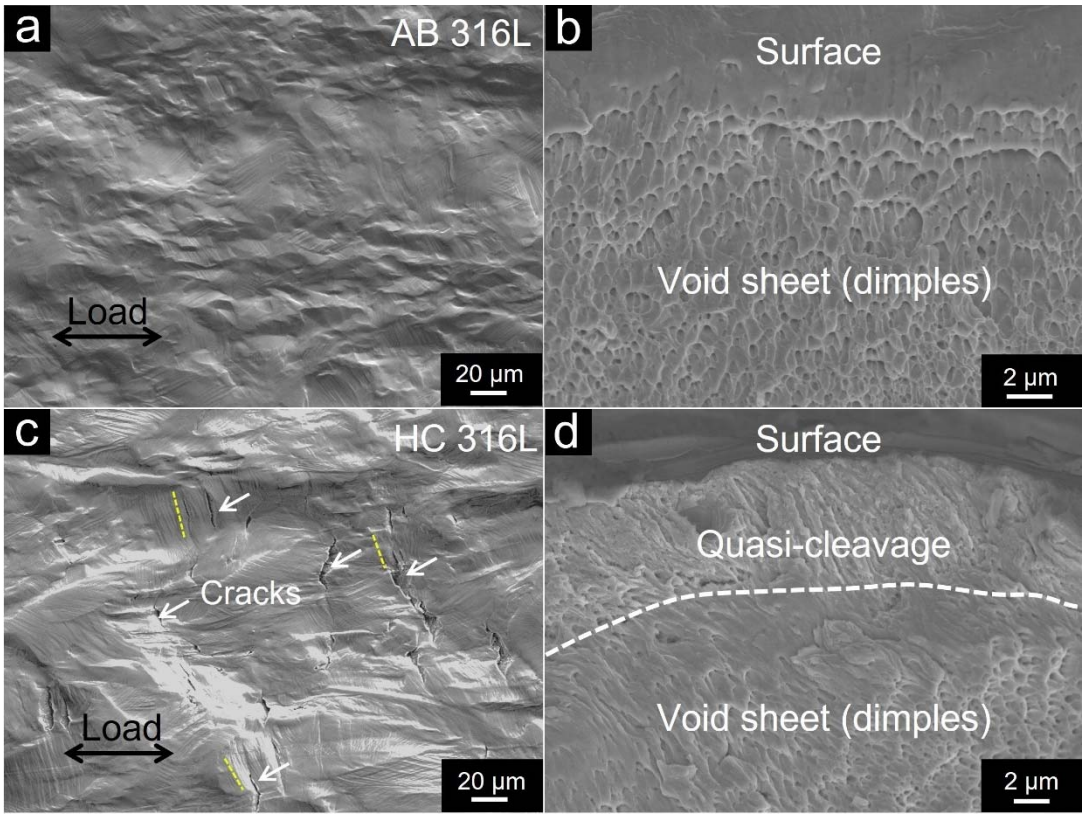

Figure 10. (a) SEM image on surface of AB 316L at the region of fracture. (b) Void sheet, consisting of voids/dimples, on the fracture surface of the AB 316L. (c) Cracks on the surface of HC 316L at the region of fracture. (d) Quasi-cleavage at the surface and void sheet within subsurface region on the fracture surface of the HC 316L. The loading direction is indicated using black arrows.

TEM was further conducted on the FIB lift-out samples fabricated from the fractured AB and HC 316L samples. As shown in Figure 11(a), deformation twins are the dominant deformation features in the AB 316L sample at high strain level (the inserted SADP confirms the twin relation). Densely distributed twins with thickness of

a few nanometers align parallelly. Similarly, twins are observed to also prevail in the fractured HC sample in Figure 11(b). The twins here are comparable to those identified in the AB sample, in terms of both size and distributions. In addition to twins, slip bands along (111) p1lanes (as indicated by the SADPs) are also frequently observed in both the AB and HC 316L (Figures 11(b) and (d)). While the slip bands appear thin and are closely spaced in the AB sample, they possess larger spacing and thicker morphology in the HC counterpart. The difference observed here is comparable to that identified in tensile samples strained to 5%, indicating that H-enhanced slip planarity persists with increasing strain.

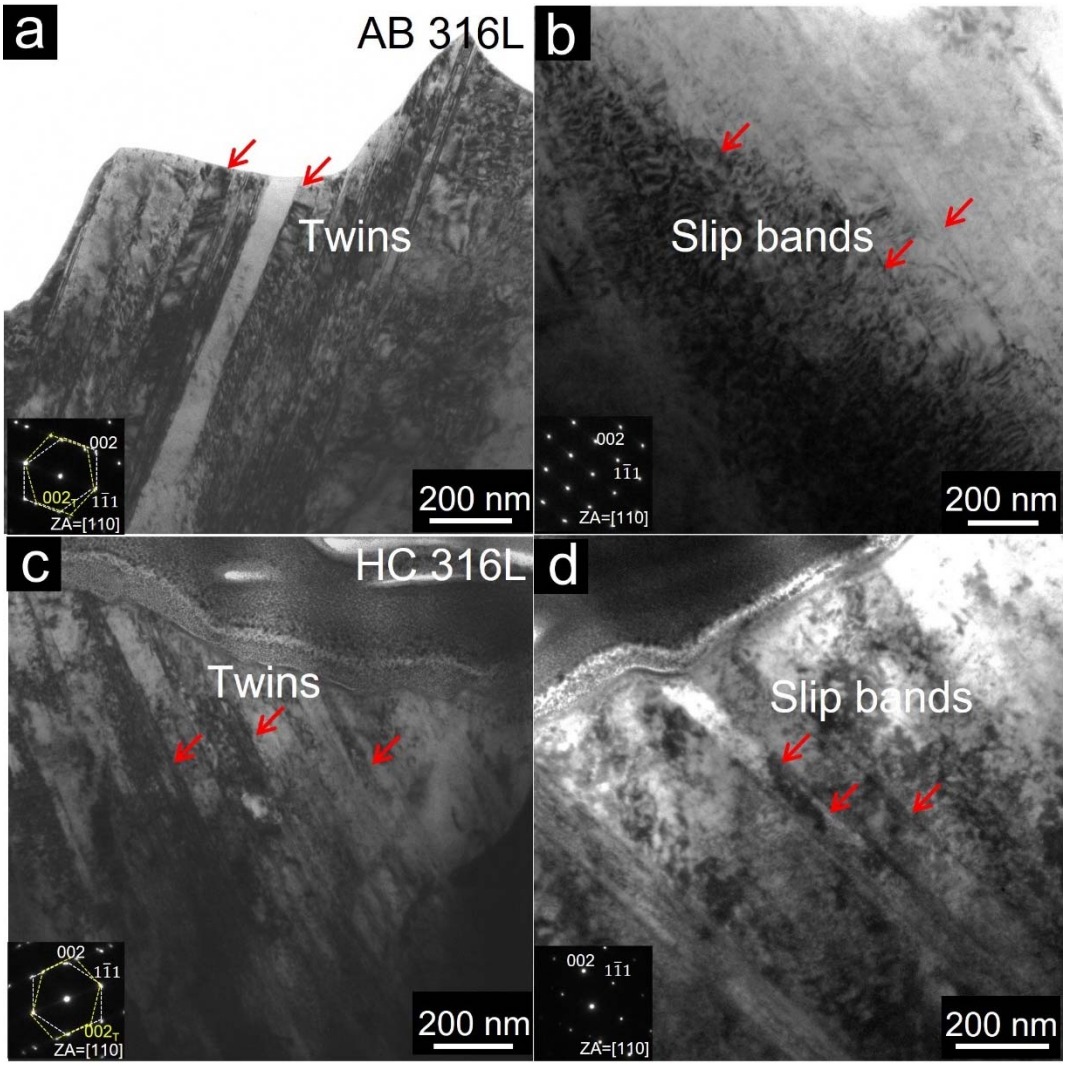

Figure 11. Deformation microstructures in the fractured tensile samples. (a) Twins and (b) slip bands in the AB 316L. (c) Twins and (d) slip bands in the HC 316L.

4. Discussion

4.1 H-induced dislocation activities

From Figures 3 and 4, a relatively more homogeneous dislocation distribution can be noted in the HC sample compared to AB sample. While dislocation networks appear well-organized with rather featureless network interiors (Figures 3(b)), some dislocations were observed outside the networks in the HC sample (Figures 3(d) and 4), making the originally well-organized dislocation networks less distinct. This demonstrates dislocation activities upon H charging without any external stress applied. Prior studies reported the formation of surface slip bands in alloys subjected to H charging in the absence of applied stress too [40-42], which was attributed to H-induced dislocation activity, including both dislocation nucleation and motion. Considering that the dislocation density remained invariant due to the H charging, as demonstrated in Figure 2, dislocation nucleation can be ruled out in the current context. Thus, dislocation motion might be the cause for the more homogeneous dislocation distribution. It has been reported that dislocation slip can be activated due to internal stress build-up due to H charging [40-42]. Barnoush *et al.* [42] proposed that dislocations in austenite phase of a duplex steel are activated by the internal stress that resulted from quench annealing treatment, and H charging facilitates dislocation motion by reducing the required stress. Wang *et al*. [40] reported that the internal stress developed due to lattice expansion (dependent on the content of dissolved H) plays a key role in triggering dislocation motion. In the present study, as no additional treatment was conducted on the sample except for H charging, the dislocation motion and resultant morphology rearrangement are attributed to internal stress due to H charging.

To estimate the magnitude of the internal stress here, TDS was conducted on the HC sample to determine the content of dissolved H. As shown in Figure 12(a), the H concentration in the HC sample is ~14.8 weight ppm (wppm). A significant gradient in H concentration exists in electrochemically charged samples [43, 44]. The local H concentration as a function of depth (x, distance from the surface) can be estimated approximately using the following relation [45]:

$$C(x,t_c) = C_0[1 - \mathrm{erf}\left(\frac{x}{2\sqrt{D_H t_c}}\right)] \quad (1)$$

where C_0 is the local H concentration at the surface, D_H is the diffusion coefficient and t_c is the H charging time. C_0 can be determined following the method by Pontini *et al*. [46]:

$$C_0 = \frac{wC_M}{4}\sqrt{\frac{\pi}{D_H t_c}} \quad (2)$$

where w is the thickness of H-charging sample, C_M is the average H concentration in the HC sample (i.e., about 14.8 wppm in the HC 316L). Taking the D_H value as 3.17×10^{-16} m^2/s at room temperature [28] and t_c=24 h, the H concentration as a function of depth is estimated and displayed in Figure 12(b). The H concentration has a maximum value of about 550 wppm at the surface, and reduces sharply with increasing depth, ultimately reaching near zero (~0.04 wppm) at ~20 μm. Recall that a transition from brittle fracture to ductile failure happens at the depth of 6–7 μm (Figure 10(d)), which corresponds to a critical H concentration of ~110 wppm.

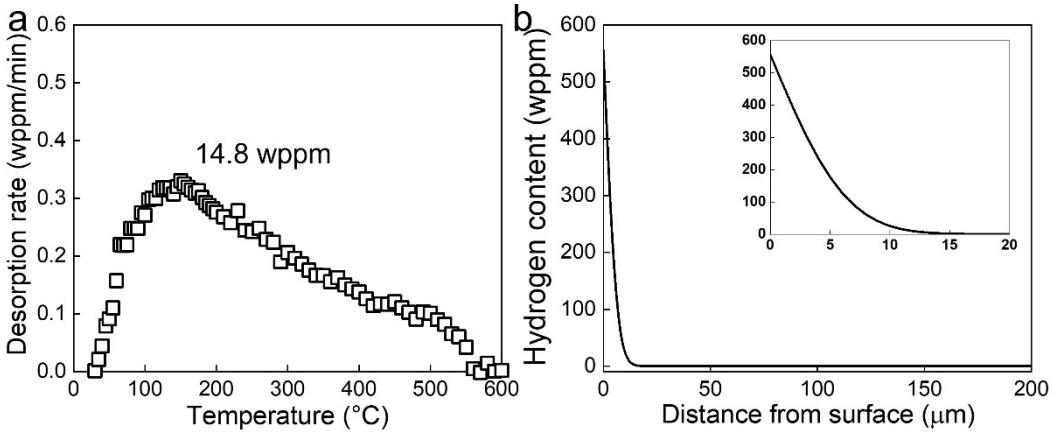

Figure 12. (a) The TDS curve of 316L after H charging. (b) The established H variation in H concentration as a function of depth (the inset showing an enlarged view of H concentration from surface to 20 μm depth).

The dislocation arrangement evolution is attributed to internal stress developed upon H charging [40-42]. According to Wang *et al.* [40], the value of internal stress, σ_i is proportional to the lattice expansion that occurs due to the H absorption. The latter factor is dependent on the atomic ratio between H and matrix, H_a/M_a, which can be estimated as follows [40]:

$$\frac{H_a}{M_a} = \frac{C_0 \times N_A / M_H}{(10^6 - C_0) \times N_A / M_A} \quad (3)$$

where N_A is the Avogadro constant, M_H and M_A are the corresponding molar masses of H and matrix, respectively. Taking the C_0 value as 550 wppm (dislocation rearrangement was limited to surface region, as evidenced in Figure 4), the estimated value of H_a/M_a near the sample surface using equation (3) is 0.015. The resultant lattice expansion due to dissolved H show linear correlation with the atomic ratio, i.e.,

$$\frac{\Delta V}{V_0} = \frac{H_a \times \Delta v}{M_a \times \Omega} \quad (4)$$

where Δv is the volume change of unit cell resulting from one hydrogen atom, and Ω is the volume of metallic atom. The calculation is simplified by adopting the $\Delta v/\Omega$ value as 0.19 (which was reported for the 310 grade stainless steel with similar austenite structures [47]). The lattice expansion calculated following the equation (4) is 0.00285. Subsequently, the internal stress developed due to lattice expansion is:

$$\sigma_i = \frac{E \times \Delta V}{V_0} \quad (5)$$

where E is the Young's Modulus of matrix (193 GPa for 316L [48]). The internal stress σ_i is then calculated to be ~550 MPa, which is ~35 MPa higher that the yield strength of L-PBF 316L. This indicates that the internal stress is high enough to activate dislocation motion, transforming the dislocation networks present at the cell boundaries in high density in the AB condition, into relatively more homogeneously-distributed morphology in the charged state. In addition, it is also possible for (sub)micron-scale H segregation, due to the appearance of dislocation networks in 316L. Chen *et al.* reported that dislocation walls containing a high-density of dislocations act as effective traps for H atoms [49]. Therefore, the localized H concentration along network boundaries, and the resultant lattice expansion and internal stress, are likely to be higher than the calculated values, which further facilitates dislocation motion upon H charging.

4.2 H-induced softening

Results of the tensile tests on bulk samples (Figure 5), together with the nanoindentation (Figure 6) and micropillar compression (Figure 7) tests, reveal the occurrence of the H-induced softening in the HC L-PBF 316L sample. While H-induced

hardening is an often reported phenomenon in literature [50, 51], H-induced softening has also been reported in different metals and alloys [29, 52]. Predicting the conditions that favor either of these two mechanisms in an alloy is complicated by various factors that are listed in Table 3, including the H content [43, 53], stress level [54-56], dislocation density [54, 57], temperature [58, 59], strain rate [53, 60], *etc*. In the literature, H-induced softening was attributed to H-enhanced dislocation motion, achieved by either increasing the dislocation mobility that occurs through a reduction of the Peierls-Nabarro potential [61, 62] or weakening of the interactions in-between dislocations and between dislocations and other defects (including impurities, solute atoms, precipitates, *etc*.) under H's elastic shielding effect [52, 63] (see Table 3 for a summary). Notably, the Peierls-Nabarro potential is important in BCC metals (such as pure iron) due to the unique screw dislocation core structures and motion modes [58, 64]. The reconstruction of core structures [65, 66] and reduction of kink (or kink pair) nucleation energy [58] upon H segregation enhances the mobility of screw dislocations, which have been experimentally identified [67]. In view of the fact that the 316L SS has pure FCC austenite structure (see Figure 1), the observed softening here is more likely to be a result of H's elastic shielding effect rather than reduction in the Peierls-Nabarro potential.

Table 3 A summary of the H-induced hardening and softening mechanisms proposed in literature. (Note that the studies reporting hydrogen-facilitated phase transformation or hydride formation are excluded- here; "P-N" refers to "Peierls-Nabarro".)

Softening	**Hardening**	**Affecting Factor**	**Material**	**Reference**
Elastic shielding	Slip planarity	–	316L	Chateau *et al*. [68]
Elastic shielding	Dragging/ Pinning	Temperature, Strain rate	Ni, Ni-C	Birnbaum & Sofronis [60]
Elastic shielding	Dragging/ Pinning	Temperature	SA508 Cl.3 steel	Wu & Kim [69]

Elastic shielding	Dragging/ Pinning	Stress	304, 316L	Murakami *et al*. [55]
Elastic shielding	Dragging/ Pinning	Stress	α-Fe, 316L	Miresmaeili *et al*. [56]
Elastic shielding	Dragging /Pinning	Stress, Vacancy concentration	Single-crystal Ni	Hachet *et al*. [70]
Elastic shielding	–	Stress, Dislocation density	X70 steel	Lee *et al*. [54]
Elastic shielding	Dragging/ Pinning	Dislocation density	β-21S Ti alloy	Tal-Gutelmacher *et al*. [71]
–	Dragging/ Pinning	H content	Low-C steel	Zhao *et al*. [43]
Reduced P-N potential	Dragging/ Pinning	H content, Strain rate	–	Kirchheim [72]
Reduced P-N potential	Dragging/ Pinning	H content, Temperature	α-Fe	Kimura & Matsui [59]

The elastic shielding effect of H has been demonstrated to weaken the interactions (typically repulsive force) in-between dislocations and between dislocations and other defects [73]. This was further verified by *in situ* TEM experiments on Al, where the directions of dislocation motion were reversed with and without H [63]. The reduced elastic interactions between dislocations lead to decreased flow stress for deformation, manifesting as H-induced softening. Although there is currently no consensus on the exact critical dislocation spacing for the H elastic shielding effect to be effective, most values proposed in available literature are in the range of tens of b (where b is the magnitude of the Burges vector) [52, 63]. Moreover, both experimental observations [54] and theoretical calculations [63] revealed that the reduced elastic interaction forces due to H shielding between dislocations increases with decreasing dislocation spacing.

This indicates that a higher dislocation density (ρ) increases the possibility for H's elastic shielding effect to occur. Due to the continuous thermal cycles and the resultant cyclic loadings inherent to the L-PBF process [25], a high-density of dislocations are formed and typically organized into networks in the L-PBF alloys (as also seen in Figure 3b). The typical ρ reported in the L-PBF alloys is at the orders of 10^{14}–10^{15} m^{-2} [74, 75], or ~2–3 orders of magnitude higher than that in their CM counterparts (typically ~10^{12} m^{-2} [76]). More importantly, the highly tangled dislocations along the cellular boundaries in the L-PBF alloys generally possess very high dislocation densities, ranging between ~10^{15} and 10^{17} m^{-2} [25, 77], resulting in an average spacing between dislocations of a few nanometers. This value is comparable to (or even smaller than) the critical value for H shielding to be operative (i.e., tens of b, which is ~0.257 nm for 316L [78]). Although the dislocations tend to disentangle and distribute more homogeneously upon H charging (Figure 3d), the dislocation density does not seem to decrease and hence the H shielding effects are expected to be largely retained. Therefore, the H-induced elastic shielding of dislocation interactions could be the main cause of the observed softening in the L-PBF 316L samples.

The above conclusion is further supported by the work hardening behavior observed in both the micropillar compression and bulk sample tensile tests. Reduced work hardening rates are identified in all the HC pillars when compared to their AB counterparts (Figure 7 and Table 1). As discussed in our recent work [21], the dislocation networks present in the L-PBF 316L alloy significantly enhance the dislocation storage and, therefore, work hardening capability in micropillars. After the H charging, nevertheless, the dislocation interactions are weakened due to the H's elastic shielding effect, resulting in the inferior work hardening capability [79]. Compared to the bulk AB 316L samples, the HC ones showed slightly lower work hardening rate θ at the early deformation stage, and θ decreases sharply as the deformation proceeds further (Figure S4). Notably, the HC samples fractured when θ is still high (~0.94 GPa), suggesting a premature failure due to the surface cracks in the HC samples, instead of conventional necking. The mechanisms for this phenomenon are further discussed in section 4.3.2.

Although the high dislocation density in the L-PBF 316L (or in any other L-PBF fabricated alloys in general) could favor the H-induced softening as observed here, it is not always the case as reported previously for the L-PBF alloys. H-induced hardening [80, 81], softening [82, 83], and invariance in strength/hardness [28, 39] have all been reported, with the extent of the changes being generally small (mostly within ~15% in strength/hardness changes). As mentioned above and that can be seen from Table 3, the factors controlling the H-induced hardening or softening are diverse and complex. It is, therefore, difficult to reach a firm conclusion as to the dominating factor for the observed H-induced softening here yet. A thorough study systematically altering various controlling factors will be necessary to obtain the quantitative thresholds for H-induced softening *vs*. hardening in any given alloy system.

4.3 H embrittlement

Compared to strength, the ductility of L-PBF 316L is more more sensitive to H charging, manifesting as the significant reduction in ε_f. The SEM and TEM images shown in Figures 8–11 demonstrate that H is a critical factor altering the microstructural evolutions upon straining and eventually resulting in the premature failure of the HC samples. Therefore, the effects of H on these aspects under tensile straining are discussed below.

4.3.1 H-enhanced slip planarity

At the early stage of plastic deformation (*e.g.*, ~5% strain), both slip bands and twins prevail in the AB and HC 316L samples. Notably, the morphologies of these deformation features vary in the H charged samples. As shown in Figure 9(a), the AB sample with 5% tensile strain is characterized by fine and dense slip bands. These slip bands, which penetrate the cell boundaries, occur along $[1\bar{1}\bar{1}]$ plane (as indicated by the corresponding SADP) with interspacing of ~0.10 μm. In contrast, the slip bands in the HC samples are coarser with an interspacing of ~0.53 μm (Figures 9(c) and S5). Such discrepancy in the slip bands is purportedly caused by the H-enhanced slip planarity. Abraham *et al*. [9] reported that slip bands featured by higher shear offset and

spacing are dominant on the surface of the plastically deformed HC 310S SS, which is similar to what we observed here in HC 316L. Similar H-enhanced slip planarity has also been identified in HC austenitic SS under nanoindentation tests [34].

H-enhanced slip planarity was also observed in the HC micropillars. Slip bands in the AB and HC 316L pillars with D=3.5 μm, characterized using both SEM and TEM, are shown in Figure 13. Densely spaced slip bands along (111) planes are observed throughout the entire pillars (Figure 13(a)). TEM analysis demonstrates that slip bands (inset is the corresponding SADP) with small interspacing prevail throughout the deformed pillar (Figure 13(b)). In contrast, the HC 316L sample is characterized by localized slip activities with slip bands occurring only along a few planes and mostly limited to the upper part of the pillar (Figure 13(c)). In Figure 13(d), the slip bands in the HC 316L pillar are coarse and separated with large interspacing, resulting from dislocation motion along a few slip planes (i.e., H-enhanced slip planarity). It should be noted that twins were not observed in either the AB or HC pillars. This could be due to the <110> loading direction that does not favor twin formation [84].

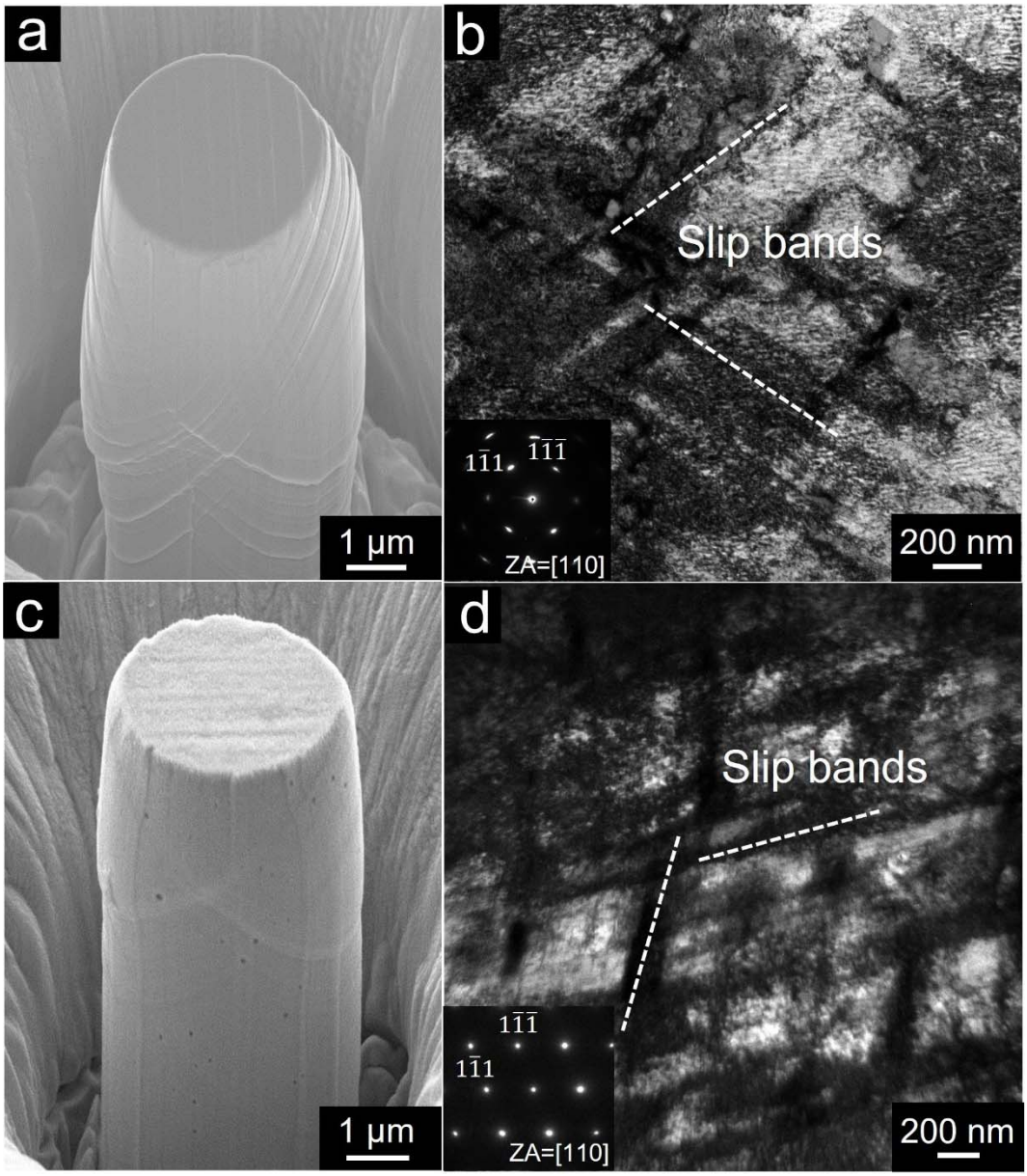

Figure 13. (a) SEM image and (b) TEM image on slip bands of AB 316L pillar. (c) SEM image and (d) TEM image on slip bands of HC 316L pillar. Insets are the corresponding SADPs, indicating only slip bands in the deformed pillars.

A key consideration for rationalizing the H-enhanced slip planarity is the reduced tendency of cross slip due to the presence of H [8, 9, 34]. As shown in Figure 9, the slip bands in the AB 316L indicate that dislocation motion occurs along numerous parallel slip planes. Notably, the appearance of dislocation networks inhibits dislocation motion [85, 86], which facilitates cross slip to some extent and further results in densely-spaced parallel slip bands [21, 87]. After H charging, H atoms preferentially occupy the dislocation cores, resulting in the formation of Cottrell-type atmospheres of H due to

the elastic stress field surrounding dislocations [60, 88]. Ferreira *et al*. provided direct experimental evidence showing that H suppress dislocation cross slip via *in situ* mechanical tests on Al [36]. Similarly, Robertson *et al*. showed that H can lock dislocations during the cross slip process with part of dislocations residing on the cross slip planes, and cross slip proceeds further with decreased H pressure [89]. Once H atoms are introduced into metallic materials, they are easily trapped by dislocations to lower the dislocation core energy [61]. Although the binding energy of H and screw dislocations is lower than that of H and edge dislocations [61], it is still high enough to suppress cross slip in metals, including Al [36], Ni [90], and austenitic SSs [9].

In addition to the binding between H and dislocation cores, some other factors could also potentially contribute to the reduced tendency of cross slip in HC L-PBF 316L of the present study. One factor is the relatively more homogeneously distributed dislocations in them. The high-density dislocations along cellular boundaries were reported to significantly inhibit dislocation motion and slip band propagation [21, 91]. The back stress exerted on mobile dislocations would decrease with reducing dislocation density within pile-ups due to H charging [92], which would also lower the possibility of cross slip. The other factor is the H-induced SFE reduction. With decreasing SFE, the spacing between partial dislocations increase, reducing the tendency of cross slip [37]. It has been shown that H induces a ~20% reduction in SFE in austenitic SSs, which was considered insufficient to exert significant effect on the tendency of cross slip [89].

It should be noted that H-enhanced slip planarity is, in fact, a mechanism contributing to H-induced hardening, as mentioned in section 4.2. The fact that we observed the indications of H-enhanced slip planarity, and yet measured a decrease in strength/hardness in HC samples, indicates the existence of a competition between H-induced softening *vs*. hardening. In the HC L-PBF 316L examined here, softening induced by H's elastic shielding effect overwhelms hardening that accrues from the H-enhanced slip planarity, manifesting as lower yield strengths in both bulk tensile samples and micropillars, as well as lower hardness determined from the nanoindentation tests. This is most likely due to both the relatively high dislocation

density in the LPBF alloy (favoring H's elastic shielding [54]) and low H content (making it less likely for H-enhanced slip planarity to be prevalent [44]) This again demonstrates that various factors could contribute to either H-induced softening or hardening, and either may prevail in a given material under certain combinations of different parameters that contribute to it.

4.3.2 H embrittlement mechanism

Various models have been proposed to rationalize the HE in different metallic materials, among which HELP [7-9] and HEDE [10, 11] are the most common. For the HC austenitic SSs, early studies reported that the strain-induced martensite formed in metastable austenite is a crucial factor for HE, since martensite can facilitate the nucleation and propagation of H-assisted cracking [28]. However, this mechanism is not valid here as the strain-induced martensite was never identified in the HC 316L, irrespective of the level of applied strain.

The premise of the HELP mechanism is that H assists deformation via enhancing dislocation mobility [7], which does occur in the alloy examined in this work and has been discussed in section 4.3.1. Upon 5% tensile strain, the dislocation activities are limited to a few slip planes, indicating the localization of plasticity. The localized plasticity is provoked by higher dislocation mobility due to H shielding effect, and possibly further enhanced by the lower resistance to dislocation motion along these planes ('dislocation channels') [35]. The localized dislocation activities on the planes could also contribute to the lower flow stress in the HC 316L (Figure 5). The H atoms have been reported to diffuse fast enough to get transferred by mobile dislocations at appropriate temperatures and strain rates (*i.e.*, the Cottrell atmosphere of H adhere to dislocation cores and move together with dislocations) [60, 88], which results in localized high H concentrations along the slip planes [93]. It has been proposed that the accumulated H atoms with sufficiently high concentrations would significantly reduce the repulsive stress fields between dislocations and other defects [60], which enhances dislocation motion and in turn the slip localization (HELP).

In addition to HELP mechanism, HEDE could also result in the observed HE in

the L-PBF 316L. In fact, a HELP-mediated HEDE model has been proposed to describe HE in various steels exposed to H atmosphere [12, 94]. Such HELP-mediated HEDE model is in line with a hydrogen-enhanced-plasticity mediated decohesion model [95], wherein H-rich regions are formed along boundaries due to localized dislocation activities (HELP) and decohesion happens with the assistant of H subsequently (HEDE). The prerequisite of HEDE is that the local H concentrations reach a critical value during the deformation process, and the dilatation of atomic lattice due to interstitial H lowers the cohesive strength of microstructures [11, 96]. As shown by the TEM image in Figure 9(d) and STEM image in Figure S5, dislocations in the HC 316L tend to pile up toward twin/slip band boundaries and grain boundaries or accumulate along the slip planes (Figure 13). Hence, although the HC samples show uniform deformation at the macroscale, the slip localization results in the inhomogeneous distributions of dislocations at the micro- or nano-scale. As mentioned earlier, H atoms could be transported by the mobile dislocations and accumulate locally, resulting in localized H-rich regions. It is reasonable to infer that such H accumulation, accompanied by dislocation pile up, occurs along the twin boundaries, slip bands, and grain boundaries. When the critical H concentration is reached, H-assisted cracking is activated. This can be further evidenced by the observation shown in Figure 10(c), where a few cracks are formed within heavily deformed regions decorated with dense slip bands/twins. In addition, these cracks are often parallel to the orientations of slip bands/twins (indicated by the yellow dashed lines). Similar results showing that microcracks initiate from twin boundaries are also reported in other HC steels [97, 98]. This indicates that *a priori* activation of HELP mechanism plays as a prerequisite for HEDE (namely HELP-mediated HEDE).

Before closing, it is instructive to briefly discuss the differences between CM and AM materials, in terms of HE in them, although it is not the key focus of this study. The most obvious and critical difference in microstructure of AM materials, or more specifically L-PBF alloys, is the dislocation networks [16, 21]. From the current results, the relatively higher dislocation density in the L-PBF 316L makes it more inclined to show H-induced softening (reduction in hardness and strength) via elastic shielding

effect. Nevertheless, in terms of ductility, which is a more critical factor from engineering application perspective in H-rich environment, the H-induced ductility loss is still severe (~30% in tensile tests in present study) and comparable to those reported for CM 316L in literature (for instance ~27% in Ref. [3]). It is noteworthy that prior studies have indicated a slightly lower H diffusivity in L-PBF 316L than in CM 316L [80, 99, 100]. This reduced diffusivity in L-PBF alloys was attributed to the high-density dislocation networks which may have a mild effect in impeding H diffusion. The lower H diffusivity in L-PBF alloys should slow down the process of H atoms migrating/segregating to stress localization region, such as crack tips, and hence could help in reducing the embrittlement caused by H to some extent. Further systematic studies to compare the H diffusivity and its effect on fatigue and fracture properties in CM and L-PBF alloys are needed to reveal the differences. Notably, special attention should be paid to the dislocations and their arrangement in AM alloys. Our earlier studies demonstrated that the high-density of dislocations in them contribute to superior strength compared to their CM counterparts [21, 87]. The current work shows that they also facilitate the H's elastic shielding effect and lead to H-induced softening.

5. Summary

An experimental investigation into the effects of H on the deformation behaviors of L-PBF 316L was conducted by recourse to tensile, micro-pillar compression, and nanoindentation tests. Combined with detailed microstructural analysis and H solubility characterization, the H effects on the deformation mechanisms and ductility loss are revealed, with the following conclusions drawn:

(1) The key deformation features are similar in the AB and HC 316L tensile samples, manifesting as prevailing slip bands and deformation twins. Due to the elastic shielding effect of H, which could be favored by the intrinsically high dislocation density in the L-PBF sample, the interactions between the dislocations are weakened, resulting in the marginally inferior hardness, strength, and work hardening capability in the HC samples.

(2) Upon H charging, internal stress rises due to H atoms occupying the interstitial sites,

which enhances dislocation motion and transforms the tangled dislocation networks into relatively more homogeneously distributed ones.

(3) A transition from the completely ductile fracture to a mixture of brittle and ductile fracture occurs upon H charging, resulting in reduced ductility in the HC samples. This H embrittlement is attributed to the HELP-mediated HEDE mechanism. As evidenced by the microstructural characterizations on tensile samples with different strains, dislocations and the H atoms travelling with them accumulate along slip bands, twin boundaries, and grain boundaries. When a critical H concentrated is reached, cracking initiates due to reduced cohesion, resulting in premature failure of HC 316L.

Acknowledgements

This work is supported by the National Natural Science Foundation of China (Grant No. 52101156). UR acknowledges the support from Structural Metal Alloys Programme (Grant No. A18B1b0061) of Agency for Science, Technology and Research (A*STAR) of Singapore. YZ thanks the support from Advanced Models for Additive Manufacturing (AM2) programme (No. M22L2b0111) of A*STAR.

References

1. P. Cotterill, The hydrogen embrittlement of metals. Prog. Mater. Sci. 9 (1961) 205-301.
2. S.K. Dwivedi, M. Vishwakarma, Hydrogen embrittlement in different materials: A review. Int. J. Hydrogen Energ. 43 (2018) 21603-21616.
3. Y. Zhao, D.-H. Lee, M.-Y. Seok, J.-A. Lee, M.P. Phaniraj, J.-Y. Suh, H.-Y. Ha, J.-Y. Kim, U. Ramamurty, J.-i. Jang, Resistance of CoCrFeMnNi high-entropy alloy to gaseous hydrogen embrittlement. Scr. Mater. 135 (2017) 54-58.
4. T. Perng, M. Johnson, C.J. Altstetter, Influence of plastic deformation on hydrogen diffusion and permeation in stainless steels. Acta Matell. 37 (1989) 3393-3397.
5. Y.S. Kim, S.H. Bak, S.S. Kim, Effect of strain-induced martensite on tensile properties and hydrogen embrittlement of 304 stainless steel. Metall. Mater. Trans. A 47 (2016) 222-230.

6. G. Han, J. He, S. Fukuyama, K.J.A.m. Yokogawa, Effect of strain-induced martensite on hydrogen environment embrittlement of sensitized austenitic stainless steels at low temperatures. Acta Mater. 46 (1998) 4559-4570.
7. C.D Beachem, A new model for hydrogen-assisted cracking (hydrogen "embrittlement"). Metall. Mater. Trans. B 3 (1972) 441-455.
8. M.L. Martin, M. Dadfarnia, A. Nagao, S. Wang, P. Sofronis, Enumeration of the hydrogen-enhanced localized plasticity mechanism for hydrogen embrittlement in structural materials. Acta Mater. 165 (2019) 734-750.
9. D.P. Abraham, C.J. Altstetter, Hydrogen-enhanced localization of plasticity in an austenitic stainless steel. Metall. Mater. Trans. A 26 (1995) 2859-2871.
10. M. Djukic, G. Bakic, V. Šijački-Žeravčić, B. Rajicic, A. Sedmak, M. Wasim, J. Perišić. The synergistic action of HELP and HEDE mechanisms of hydrogen embrittlement in steels. in Research Symposium on Hydrogen-Materials Interactions, Kyushu University: Fukuoka, Japan. 2021.
11. R.A. Oriani, P.H. Josephic, Equilibrium aspects of hydrogen-induced cracking of steels. Acta Matell. 22 (1974) 1065-1074.
12. M.B. Djukic, G.M. Bakic, V. Sijacki Zeravcic, A. Sedmak, B. Rajicic, The synergistic action and interplay of hydrogen embrittlement mechanisms in steels and iron: Localized plasticity and decohesion. Eng. Fract. Mech. 216 (2019) 106528.
13. S.-H. Li, P. Kumar, S. Chandra, U. Ramamurty, Directed energy deposition of metals: processing, microstructures, and mechanical properties. Inter. Mater. Rev. 68 (2023) 605-647.
14. T. DebRoy, H.L. Wei, J.S. Zuback, T. Mukherjee, J.W. Elmer, J.O. Milewski, A.M. Beese, A. Wilson-Heid, A. De, W. Zhang, Additive manufacturing of metallic components – Process, structure and properties. Pro. Mater. Sci. 92 (2018) 112-224.
15. S. Wei, C. Hutchinson, U. Ramamurty, Mesostructure engineering in additive manufacturing of alloys. Scr. Mater. 230 (2023) 115429.
16. Y.M. Wang, T. Voisin, J.T. McKeown, J. Ye, N.P. Calta, Z. Li, Z. Zeng, Y. Zhang, W. Chen, T.T. Roehling, R.T. Ott, M.K. Santala, P.J. Depond, M.J. Matthews, A.V. Hamza, T. Zhu, Additively manufactured hierarchical stainless steels with high strength and ductility. Nat. Mater. 17 (2018) 63-71.
17. P. Kumar, O. Prakash, U. Ramamurty, Micro-and meso-structures and their influence on mechanical properties of selectively laser melted Ti-6Al-4V. Acta Mater. 154 (2018) 246-260.
18. D. Kong, C. Dong, X. Ni, L. Zhang, H. Luo, R. Li, L. Wang, C. Man, X. Li,

Superior resistance to hydrogen damage for selective laser melted 316L stainless steel in a proton exchange membrane fuel cell environment. Corros. Sci. 166 (2020) 108425.

19. L. Claeys, L. Deconinck, K. Verbeken, T. Depover, Effect of additive manufacturing and subsequent heat and/or surface treatment on the hydrogen embrittlement sensitivity of 316L austenitic stainless steel. Int. J. Hydrogen Energ. 48 (2023) 36142-36157.
20. Z. Zhou, K. Zhang, Y. Hong, H. Zhu, W. Zhang, Y. He, C. Zhou, J. Zheng, L. Zhang, The dependence of hydrogen embrittlement on hydrogen transport in selective laser melted 304L stainless steel. Inter. J. Hydrogen Energ. 46 (2021) 16153-16163.
21. S.-H. Li, Y. Zhao, J. Radhakrishnan, U. Ramamurty, A micropillar compression investigation into the plastic flow properties of additively manufactured alloys. Acta Mater. 240 (2022) 118290.
22. Z. Sun, X. Tan, S.B. Tor, W.Y. Yeong, Selective laser melting of stainless steel 316L with low porosity and high build rates. Mater. Des. 104 (2016) 197-204.
23. N. Narita, C.J. Altstetter, H.K. Birnbaum, Hydrogen-related phase transformations in austenitic stainless steels. Metall. Trans. A 13 (1982) 1355-1365.
24. H.-J. Cho, Y. Cho, H. Gwon, S. Lee, S.S. Sohn, S.-J. Kim, Effects of Ni/Cu replacement on improvement of tensile and hydrogen-embrittlement properties in austenitic stainless steels. Acta Mater. 235 (2022) 118093.
25. G. Wang, H. Ouyang, C. Fan, Q. Guo, Z. Li, W. Yan, Z. Li, The origin of high-density dislocations in additively manufactured metals. Mater. Res. Lett. 8 (2020) 283-290.
26. J. Suryawanshi, K.G. Prashanth, U. Ramamurty, Mechanical behavior of selective laser melted 316L stainless steel. Mater. Sci. Eng. A 696 (2017) 113-121.
27. D. Kong, C. Dong, X. Ni, L. Zhang, J. Yao, C. Man, X. Cheng, K. Xiao, X. Li, Mechanical properties and corrosion behavior of selective laser melted 316L stainless steel after different heat treatment processes. J. Mater. Sci. Technol. 35 (2019) 1499-1507.
28. D.-H. Lee, B. Sun, S. Lee, D. Ponge, E.A. Jägle, D. Raabe, Comparative study of hydrogen embrittlement resistance between additively and conventionally manufactured 304L austenitic stainless steels. Mater. Sci. Eng. A 803 (2021) 140499.
29. Y. Zhao, M.-Y. Seok, D.-H. Lee, J.-A. Lee, J.-Y. Suh, J.-i. Jang, Hydrogen-induced softening in nanocrystalline Ni investigated by nanoindentation. Philos. Mag. 96 (2016) 3442-3450.

30. S. Wei, Y. Zhao, J.-i. Jang, U. Ramamurty, Rate-dependent mechanical behavior of single-, bi-, twinned-, and poly-crystals of CoCrFeNi high-entropy alloy. J. Mater. Sci. Technol. 120 (2022) 253-264.
31. S.-H. Li, W.-Z. Han, J. Li, E. Ma, Z.-W. Shan, Small-volume aluminum alloys with native oxide shell deliver unprecedented strength and toughness. Acta Mater. 126 (2017) 202-209.
32. X. Zhang, K.E. Aifantis, A.H.W. Ngan, Interpreting the stress–strain response of Al micropillars through gradient plasticity, Mater. Sci. Eng. A 591 (2014) 38-45.
33. A.S. Schneider, D. Kiener, C.M. Yakacki, H.J. Maier, P.A. Gruber, N. Tamura, M. Kunz, A.M. Minor, C.P. Frick, Influence of bulk pre-straining on the size effect in nickel compression pillars. Mater. Sci. Eng. A 559 (2013) 147-158.
34. K. Nibur, D. Bahr, B. Somerday, Hydrogen effects on dislocation activity in austenitic stainless steel. Acta Mater. 54 (2006) 2677-2684.
35. S. Li, N. Gao, W. Han, In-situ study of initiation and extension of nano-thick defect-free channels in irradiated nickel. J. Mater. Sci. Technol. 58 (2020) 114-119.
36. P.J. Ferreira, I.M. Robertson, H.K. Birnbaum, Hydrogen effects on the character of dislocations in high-purity aluminum. Acta Mater. 47 (1999) 2991-2998.
37. X.W. Zhou, C. Nowak, R.S. Skelton, M.E. Foster, J.A. Ronevich, C. San Marchi, R.B. Sills, An Fe–Ni–Cr–H interatomic potential and predictions of hydrogen-affected stacking fault energies in austenitic stainless steels. Int. J. Hydrogen Energ. 47 (2022) 651-665.
38. Z.-H. Lai, Y.-T. Lin, Y.-H. Sun, J.-F. Tu, H.-W. Yen, Hydrogen-induced ductilization in a novel austenitic lightweight TWIP steel, Scr. Mater. 213 (2022) 114629.
39. D.-H. Lee, Y. Zhao, S.Y. Lee, D. Ponge, E.A. Jägle, Hydrogen-assisted failure in Inconel 718 fabricated by laser powder bed fusion: The role of solidification substructure in the embrittlement. Scr. Mater. 207 (2022) 114308.
40. D. Wang, X. Lu, Y. Deng, D. Wan, Z. Li, A. Barnoush, Effect of hydrogen-induced surface steps on the nanomechanical behavior of a CoCrFeMnNi high-entropy alloy revealed by in-situ electrochemical nanoindentation. Intermetallics 114 (2019) 106605.
41. A.S. Ebner, S. Brinckmann, E. Plesiutschnig, H. Clemens, R. Pippan, V. Maier-Kiener, A modified electrochemical nanoindentation setup for probing hydrogen-material interaction demonstrated on a nickel-based alloy. JOM 72 (2020) 2020-2029.
42. A. Barnoush, M. Zamanzade, H. Vehoff, Direct observation of hydrogen-enhanced plasticity in super duplex stainless steel by means of in situ electrochemical

methods. Scr. Mater. 62 (2010) 242-245.
43. Y. Zhao, M.-Y. Seok, I.-C. Choi, Y.-H. Lee, S.-J. Park, U. Ramamurty, J.-Y. Suh, J.-i. Jang, The role of hydrogen in hardening/softening steel: Influence of the charging process. Scr. Mater. 107 (2015) 46-49.
44. Y. Zhao, J.-M. Park, D.-H. Lee, E.J. Song, J.-Y. Suh, U. Ramamurty, J.-i. Jang, Influences of hydrogen charging method on the hydrogen distribution and nanomechanical properties of face-centered cubic high-entropy alloy: A comparative study. Scr. Mater. 168 (2019) 76-80.
45. J. Crank, The mathematics of diffusion. 1979: Oxford university press.
46. A.E. Pontini, J.D. Hermida, X-ray diffraction measurement of the stacking fault energy reduction induced by hydrogen in an AISI 304 steel. Scr. Mater. 37 (1997) 1831-1837.
47. D. Ulmer, C.J. Altstetter, Phase relations in the hydrogen-austenite system. Acta Matell. Mater. 41 (1993) 2235-2241.
48. K. Essa, P. Jamshidi, J. Zou, M.M. Attallah, H. Hassanin, Porosity control in 316L stainless steel using cold and hot isostatic pressing. Mater. Des. 138 (2018) 21-29.
49. L. Chen, X. Xiong, X. Tao, Y. Su, L. Qiao, Effect of dislocation cell walls on hydrogen adsorption, hydrogen trapping and hydrogen embrittlement resistance. Corros. Sci. 166 (2020) 108428.
50. C. Sanmarchi, Effects of alloy composition and strain hardening on tensile fracture of hydrogen-precharged type 316 stainless steels. Int. J. Hydrogen Energ. 33 (2008) 889-904.
51. K.M. Bertsch, A. Nagao, B. Rankouhi, B. Kuehl, D.J. Thoma, Hydrogen embrittlement of additively manufactured austenitic stainless steel 316 L. Corros. Sci. 192 (2021) 109790.
52. Y. Jagodzinski, H. Hänninen, O. Tarasenko, S. Smuk, Interaction of hydrogen with dislocation pile-ups and hydrogen induced softening of pure iron. Scr. Mater. 43 (2000) 245-251.
53. R. Kirchheim, Solid solution softening and hardening by mobile solute atoms with special focus on hydrogen. Scr. Mater. 67 (2012) 767-770.
54. D.-H. Lee, J.-A. Lee, M.-Y. Seok, U.B. Baek, S.H. Nahm, J.-i. Jang, Stress-dependent hardening-to-softening transition of hydrogen effects in nanoindentation of a linepipe steel. Int. J. Hydrogen Energ. 39 (2014) 1897-1902.
55. Y. Murakami, T. Kanezaki, Y. Mine, Hydrogen Effect against Hydrogen Embrittlement. Metall. Mater. Trans. A 41 (2010) 2548-2562.
56. R. Miresmaeili, L. Liu, H. Kanayama, A possible explanation for the contradictory results of hydrogen effects on macroscopic deformation. Int. J. Press. Vessel. Pip.

99-100 (2012) 34-43.
57. E. Tal-Gutelmacher, A. Pundt, R. Kirchheim, The effect of residual hydrogen on hydrogenation behavior of titanium thin films. Scr. Mater. 62 (2010) 709-712.
58. M. Itakura, H. Kaburaki, M. Yamaguchi, T. Okita, The effect of hydrogen atoms on the screw dislocation mobility in bcc iron: A first-principles study. Acta Mater. 61 (2013) 6857-6867.
59. H. Kimura, H. Matsui, Mechanism of hydrogen-induced softening and hardening in iron. Scr. Matell. 21 (1987) 319-324.
60. H.K. Birnbaum, P. Sofronis, Hydrogen-enhanced localized plasticity—a mechanism for hydrogen-related fracture. Mater. Sci. Eng. A 176 (1994) 191-202.
61. G. Lu, Q. Zhang, N. Kioussis, E. Kaxiras, Hydrogen-enhanced local plasticity in aluminum: an ab initio study. Phys. Rev. Lett. 87 (2001) 095501.
62. I.H. Katzarov, D.L. Pashov, A.T. Paxton, Hydrogen embrittlement I. Analysis of hydrogen-enhanced localized plasticity: Effect of hydrogen on the velocity of screw dislocations in α-Fe. Phys. Rev. Lett. 1 (2017) 033602.
63. P.J. Ferreira, I.M. Robertson, H.K. Birnbaum, Hydrogen effects on the interaction between dislocations. Acta Mater. 46 (1998) 1749-1757.
64. P.-J. Yang, Q.-J. Li, T. Tsuru, S. Ogata, J.-W. Zhang, H.-W. Sheng, Z.-W. Shan, G. Sha, W.-Z. Han, J. Li, E. Ma, Mechanism of hardening and damage initiation in oxygen embrittlement of body-centred-cubic niobium. Acta Mater. 168 (2019) 331-342.
65. P.P.P.O. Borges, E. Clouet, L. Ventelon, Ab initio investigation of the screw dislocation-hydrogen interaction in bcc tungsten and iron. Acta Mater. 234 (2022) 118048.
66. Y.-H. Li, H.-B. Zhou, F. Gao, G. Lu, G.-H. Lu, F. Liu, Hydrogen induced dislocation core reconstruction in bcc tungsten. Acta Mater. 226 (2022) 117622.
67. L. Huang, D. Chen, D. Xie, S. Li, Y. Zhang, T. Zhu, D. Raabe, E. Ma, J. Li, Z. Shan, Quantitative tests revealing hydrogen-enhanced dislocation motion in α-iron. Nat. Mater. 22 (2023) 710-716.
68. J. Chateau, D. Delafosse, T. Magnin, Numerical simulations of hydrogen–dislocation interactions in fcc stainless steels.: part II: hydrogen effects on crack tip plasticity at a stress corrosion crack. Acta Mater. 50 (2002) 1523-1538.
69. X.Q. Wu, I.S. Kim, Effects of strain rate and temperature on tensile behavior of hydrogen-charged SA508 Cl. 3 pressure vessel steel. Mater. Sci. Eng. A 348 (2003) 309-318.
70. G. Hachet, A. Oudriss, A. Barnoush, T. Hajilou, D. Wang, A. Metsue, X. Feaugas, Antagonist softening and hardening effects of hydrogen investigated using

nanoindentation on cyclically pre-strained nickel single crystal. Mater. Sci. Eng. A 803 (2021) 140480.
71. E. Tal-Gutelmacher, D. Eliezer, Th. Boellinghaus, Investigation of hydrogen-deformation interactions in β-21S titanium alloy using thermal desorption spectroscopy. J. Alloys Compd. 440 (2007) 204-209.
72. R. Kirchheim, Solid solution softening and hardening by mobile solute atoms with special focus on hydrogen. Scr. Mater. 67 (2012) 767-770.
73. S. Wang, N. Hashimoto, Y. Wang, S. Ohnuki, Activation volume and density of mobile dislocations in hydrogen-charged iron. Acta Mater. 61 (2013) 4734-4742.
74. F. Wei, B. Cheng, P. Kumar, P. Wang, J.J. Lee, H.L. Seng, K.H. Cheong, K.B. Lau, C.C. Tan, A comparative study of additive manufactured and wrought SS316L: Pre-existing dislocations and grain boundary characteristics. Mater. Sci. Eng. A 833 (2022) 142546.
75. Y.J. Yin, J.Q. Sun, J. Guo, X.F. Kan, D.C. Yang, Mechanism of high yield strength and yield ratio of 316 L stainless steel by additive manufacturing. Mater. Sci. Eng. A 744 (2019) 773-777.
76. G.K. Williamson, R.E. Smallman, Dislocation densities in some annealed and cold-worked metals from measurements on the X-ray debye-scherrer spectrum. Philos. Mag. 1 (1956) 34-46.
77. J. Kwon, G.M. Karthik, Y. Estrin, H.S. Kim, Constitutive modeling of cellular-structured metals produced by additive manufacturing. Acta Mater. 241 (2022) 118421.
78. Z. Li, B. He, Q. Guo, Strengthening and hardening mechanisms of additively manufactured stainless steels: The role of cell sizes. Scr. Mater. 177 (2020) 17-21.
79. A.M. Brass, J. Chêne, Hydrogen uptake in 316L stainless steel: Consequences on the tensile properties. Corros. Sci. 48 (2006) 3222-3242.
80. J.-M. Park, Y. Zhao, T. Voisin, D.-H. Lee, S.-i. Komazaki, Y. Ko, D.-I. Kim, J.-Y. Suh, H.N. Han, Y.M. Wang, U. Ramamurty, J.-i. Jang, Hydrogen uptake and its influence in selective laser melted austenitic stainless steel: A nanoindentation study. Scr. Mater. 194 (2021) 113718.
81. Y.-T. Lin, X. An, Z. Zhu, M.L.S. Nai, C.-W. Tsai, H.-W. Yen, Effect of cell wall on hydrogen response in CoCrFeMnNi high-entropy alloy additively manufactured by selective laser melting. J. Alloys Compd. 925 (2022) 166735.
82. Z. Fu, B. Yang, K. Gan, D. Yan, Z. Li, G. Gou, H. Chen, Z. Wang, Improving the hydrogen embrittlement resistance of a selective laser melted high-entropy alloy via modifying the cellular structures. Corros. Sci. 190 (2021) 109695.
83. J. Xu, Z. Hao, Z. Fu, X. He, H. Wang, G. Xu, Hydrogen embrittlement behavior

of selective laser-melted Inconel 718 alloy. J. Mater. Res. Technol. 23 (2023) 359-369.
84. X. Wang, J.A. Muñiz-Lerma, M. Attarian Shandiz, O. Sanchez-Mata, M. Brochu, Crystallographic-orientation-dependent tensile behaviours of stainless steel 316L fabricated by laser powder bed fusion. Mater. Sci. Eng. A 766 (2019) 138395.
85. S.-H. Li, Y. Zhao, K.B. Lau, P. Wang, R. Upadrasta, Micropillar compression investigation on the mechanical behavior of Ni manufactured using laser powder bed fusion. Mater. Sci. Eng. A 879 (2023) 145269.
86. S.-H. Li, Y. Zhao, U. Ramamurty, Role of the solidification cells on the yield strength of the Al-Si-Mg alloy manufactured using laser powder bed fusion: A micropillar compression study. Scr. Mater. 234 (2023) 115566.
87. S.-H. Li, Y. Zhao, P. Kumar, U. Ramamurty, Effect of initial dislocation density on the plastic deformation response of 316L stainless steel manufactured by directed energy deposition. Mater. Sci. Eng. A 851 (2022) 143591.
88. J. Tien, A.W. Thompson, I. Bernstein, R.J. Richards, Hydrogen transport by dislocations. Metall. Trans. A 7 (1976) 821-829.
89. I.M. Robertson, The effect of hydrogen on dislocation dynamics. Eng. Fract. Mech. 68 (2001) 671-692.
90. W.A. McINTEER, A.W. Thompson, I. M. Bernstein, The effect of hydrogen on the slip character of nickel. Acta Metall. 28 (1980) 887-894.
91. L. Liu, Q. Ding, Y. Zhong, J. Zou, J. Wu, Y.-L. Chiu, J. Li, Z. Zhang, Q. Yu, Z. Shen, Dislocation network in additive manufactured steel breaks strength–ductility trade-off. Mater. Today 21 (2018) 354-361.
92. R. Schouwenaars, M. Seefeldt, P. Van Houtte, The stress field of an array of parallel dislocation pile-ups: Implications for grain boundary hardening and excess dislocation distributions. Acta Mater. 58 (2010) 4344-4353.
93. D.-H. Lee, J.Y. Jung, K.H. Lee, S.Y. Lee, Y. Zhao, K.B. Lau, P. Wang, U. Ramamurty, Distinct effects of in-situ and ex-situ hydrogen charging methods on the mechanical behavior of CoCrFeNi high-entropy alloy fabricated by laser-powder bed fusion. J. Alloys Compd. 940 (2023) 168858.
94. M. Dadfarnia, A. Nagao, S. Wang, M.L. Martin, B.P. Somerday, P. Sofronis, Recent advances on hydrogen embrittlement of structural materials. Int. J. Fract. 196 (2015) 223-243.
95. A. Nagao, M. Dadfarnia, B.P. Somerday, P. Sofronis, R.O. Ritchie, Hydrogen-enhanced-plasticity mediated decohesion for hydrogen-induced intergranular and "quasi-cleavage" fracture of lath martensitic steels, J. Mech. Phys. Solids 112 (2018) 403-430.

96. M.B. Djukic, V.S. Zeravcic, G. Bakic, A. Sedmak, B. Rajicic, Hydrogen embrittlement of low carbon structural steel. Proc. Mater. Sci. 3 (2014) 1167-1172.
97. Y. Hong, C. Zhou, S. Wagner, S. Schlabach, A. Pundt, L. Zhang, J. Zheng, Strain-induced twins and martensite: Effects on hydrogen embrittlement of selective laser melted (SLM) 316 L stainless steel. Corros. Sci. 208 (2022) 110669.
98. Y. Wang, X. Wang, J. Gong, L. Shen, W. Dong, Hydrogen embrittlement of catholically hydrogen-precharged 304L austenitic stainless steel: Effect of plastic pre-strain. Int. J. Hydrogen Energ. 39 (2014) 13909-13918.
99. J. Lin, F. Chen, F. Liu, D. Xu, J. Gao, X. Tang, Hydrogen permeation behavior and hydrogen-induced defects in 316L stainless steels manufactured by additive manufacturing. Mater. Chem. Phys. 250 (2020) 123038.
100. D.-H. Lee, Y.H. An, Y. Zhao, J.H. Lee, H.Y. Kim, Y.S. Kim, S.Y. Lee, A novel methodology to estimate hydrogen diffusivity and its applications in revealing hydrogen effects in CoCrNi medium-entropy alloy versus 316L stainless steel. Int. J. Plast. 169 (2023) 103737.